CHAPTER 2

Literature Survey

2.1 Classifications of Stainless Steels and Effects of Alloying Elements on Their Structure and Properties

Alloying elements and their relative proportions, in relation to their nickel and chromium equivalence in stainless steels, result in useful differences in structure and properties, hence expanding the range of applications (Lippold and Kotecki, 2005). The binary phase diagram of the major elements Fe and Cr in Figure 2.1 can be used to illustrate possible phases that may be present at various temperatures. Two outstanding features in this diagram are the presence of sigma phase at around 50% Cr and gamma-loop at above 800 degrees Celsius (Llewellyn and Hudd, 2000).

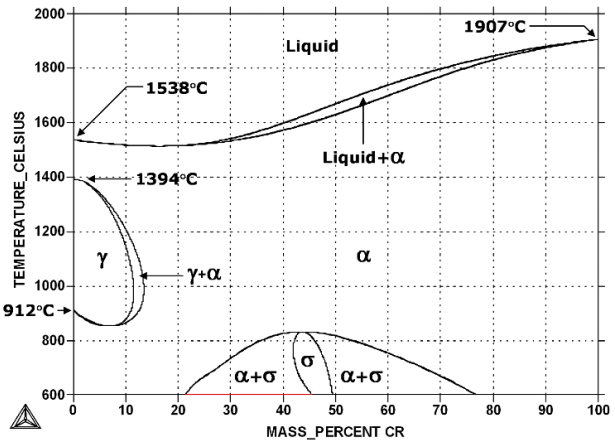

Figure 2.1 Illustration of Fe-Cr Phase Diagram
(after http://www.calphad.com/graphs/Fe-Cr%20Phase%20Diagram.gif)

The sigma phase is hard and brittle intermetallic compound mainly consists of Fe and Cr (Klemetti*et al*., 1984). It can exist if chromium proportion in alloy is less than 50% and usually formed in the temperature range from 750 to 820 ℃ especially when strong ferrite stabilizers, Si or Mo, are also present (Hsieh and Wu, 2012). It was found to influence susceptibility to corrosion resistance of stainless steels as well as mechanical properties (Baddoo, 2008).

The gamma loop is the small restricted area of fcc γ-iron formation surrounded by ferrite phase field (Messler, 1999). Chromium is a bcc ferrite stabilizer. If chromium content is increased, then the high- and low-temperature δ and α fields expand (Krauss, 2005). The amounts in excess of 12% by weight of chromium is the key to achieving stainless behaviour. Corrosion resistance of stainless steels results from the very thin chromium oxide protective layer on the surface which can rapidly self-healing when damage (Lee *et al*., 2013).

Stainless steels can be classified in terms of their dominant matrix microstructures as summarized in Table 2.1, which also indicates potential for hardening together with ferromagnetic response (Cardarelli, 2008 and Lo *et al*., 2009).

Table 2.1 Classification of Stainless Steels by Dominant Microstructure

Type of Stainless Steels	**Composition**	**Hardenability and Ferromagnetic Response**
Martensitic	12-18 wt% Cr, carbon < 1.2 wt%	H/M
Ferritic	17-30 wt% Cr, carbon < 1.2 wt%	H/M
Austenitic	18-26 wt% Cr; 8-20 wt% Ni	NH/NM
Duplex (Austenoferritic)	22-25 wt% Cr, 4-7 wt% Ni, 0.3-4 wt% Mo	NH/M
Precipitation hardening (P-H)	12-30 wt% Cr (Al, Ti, Mo)	H/M
Mn-N substituted austenitic stainless steels	16-18 wt% Cr, 3-6 wt% Ni, 5-8 wt% Mn	NH/NM

Remarks: H = hardenable, NH = non-hardenable, M = magnetic and NM = non-magnetic

Martensitic stainless steels are processed via quenching and tempering in order to provide high hardness (Gavriljuk*et al*., 2008). Main purpose in careful control of alloy compositions in austenitic, ferritic and duplex stainless steels is to avoid the formation of detrimental phases that can reduce corrosion resistance (Lo *et al*., 2009). If higher strength is needed, cold work and strain induction can be applied to austenitic stainless steels (Cardarelli, 2008). Duplex stainless steels are the Fe-Cr-Ni two-phase alloys (Davis, 1994). They have higher yield strength and provide greater resistance to stress corrosion cracking (SCC) than austenite grade (Chen *et al*., 1999). Their superior properties are in terms of higher strength, better corrosion resistance to chloride environment, hence better immunity to SCC and lesser prone to pitting (Morello*et al*., 2003).

In general, the amount of carbon in most grades of stainless steels is usually keep at below 0.1 wt%, except in martensitic grade (Lippold and Kotecki, 2005). Presence of carbon in solution have a function to provide interstitial strength at low temperature (Davis, 1994). However, if there is sufficient carbon, it can combine with predominant

metallic elements (M) such as chromium, iron or molybdenum to form complex carbides (MC type *i.e.* M_7C_3 or $M_{23}C_6$) dispersed in the matrix of stainless steels, especially in grain boundary regions (Tang, 2005, Gavriljuk*et al*., 2008). These carbides are detrimental since they increase susceptibility to grain boundary attack and affected the degradation in corrosion resistance (Gaverick, 2011). In order to obtain better prevention of $M_{23}C_6$ precipitation, carbon concentration levels have been controlled not to exceed 0.04 wt% in low-carbon or "L" grade stainless steels (Kokawa, 1994).

Nitrogen is a strong austenite stabilizer which reduces the tendency for δ-ferrite formation at high temperature and for α'-martensite formation at low temperature (Ilola *et al*., 1998 and de Abreu *et al*., 2007). It has a strong capability for solid solution strengthening similar to carbon (Lippold, 2015). Hence, the amount of nitrogen to be added in stainless steels is normally controlled at no higher than 0.15 wt% (Padhy *et al*., 2010). But in exceptional cases as in duplex stainless steel, nitrogen concentration is allowed to increase as high as 0.3 wt%. Sometimes nitrogen has been added to shielding gas to benefit the level of nitrogen concentration in weld metal (Deepashri *et al*., 2006).However, if the amount of nitrogen steels exceeds the limit of solubility, detrimental Cr_2N will be found to precipitate in ferrite phase (Arata *et al*., 1976). This is a brittle phase like MC compounds and makes stainless steels more susceptibility to corrosion, less durable and can reduce their mechanical properties (Di Schino and Kenny, 2002).

The amount of chromium in stainless steels is varied in order to achieve the desired matrix structure with respect to other alloying additives that may be present, for example 12 wt% in martensitic, 17 wt% in ferritic and 18 wt% in austentic stainless steels (Llewellyn and Hudd, 2000). Figure 2.1 shows how increase in Cr content reduces the formation of the fcc austenite phase to the area within the γloop. Chromium has several functions in the composition of stainless steels, not only as corrosion protection aid in oxidizing environment but also as a strong ferrite promoter/stabilizer (Sudesh *et al*., 2006 and Lo *et al*., 2009).

On the other hand, nickel is the main austenite phase promoter and stabilizer, when present in sufficient amount at ambient or even at lower temperatures (Di Schino

et al., 2000). The presence of nickel in stainless steels provides strength, ductility and toughness at low temperature (Davis, 1994). Generally, nickel contents range from 8 to 20 wt% in proportion with chromium (between 18 to 25 wt%) for the 300 series (Grim, 2000). In terms of contribution to corrosion resistance, even though it has no direct influence to the development of passive layer as chromium, it still helps to improve corrosion resistance especially in acid environment (Llewellyn and Hudd, 2000).

Manganese is present in most steels. In the conventional 300 series austenitic stainless steels, its proportion is limited to 1 to 2 wt% (Lippold and Kotecki, 2005). Mn provides de-oxidation in melts and by forming MnS avoids hot cracking due formation of iron sulfide (FeS). It can however generate hot shortness problems at elevate temperature or in the recrystallization during welding (Kotecki, 2000). It had also been found that Mn increases susceptibility to pitting formation due manganese sulfide (MnS) compound at pit sites (Pardo *et al*., 2008).

Molybdenum is a ferrite promoter in the microstructure of several stainless steels (Arata *et al*., 1976). It has been added in ferritic, austenitic and duplex in the amount around 6 wt% or a little higher to improve pitting and crevice corrosion resistance particularly with nitrogen (Jargelius-Pettersson, 1999). In terms of mechanical properties improvement, yield strength and hardening at high temperature can be achieved when added in the composition around 0.5 wt% (Blondeu, 2008).

Silicon has a function similar to molybdenum as previously mentioned, but still inconclusive (Grimm, 2000). Normally addition of silicon in stainless steel composition ranges from 1 to 3 wt% to improve oxidation resistance at elevated temperatures (Lippold and Kotecki, 2005). Si can have damaging effects due to it tendency to form intermetallic compounds of iron silicides and to promote Cr_3Fe and sigma phase due to segregation during solidification (Hsieh, 2012). Therefore, in austenitic grades, the maximum amount of silicon to be added is usually at 1 wt% or lower (Klemtti*et al*., 1984; Lippold and Kotecki, 2005)

Normally, when molybdenum is present, silicon and copper are usually added altogether to improve corrosion resistance in acid environments (Lippold and Kotecki, 2005). Sourisseu *et al*. (2005) has found a beneficial effect of copper sulfide (CuS_2)

formation that inhibited sulfur compound formation at surface. The study of Parvathavathini *et al*. (2009) indicated that copper decreased the anodic dissolution rate of stainless steels in acid electrolyte due to precipitation of obstructive metallic copper. Intergranular corrosion resistance can be increased by copper addition in stainless steels due to inhibition of chromium depletion (Gonzalez *et al*., 2003).

The stability of austenite and ferrite phases in stainless steels depends on two important facts (Llewellyn and Hudd, 2000). The first is a balance of composition to signify microstructure of stainless steels at high temperature and transformation during cooling to room temperature. Small amounts of alloying elements as titanium and niobium help promote ferrite phase as well as carbide and nitride complex formation (Llewellyn and Hudd, 2000). The main role of Ti and Nb is to prevent chromium carbides formation. To maintain austenite stability, the martensitic transformation temperature (M_s) that can lead to the formation of ferrite must be lowered to sub-zero levels (Kotecki, 2000). The martensite start temperature can be predicted from composition by Eq. 2.1:

$$M_s(℃) = 539 - 423C - 30.4Mn - 17.7Ni - 12.1Cr - 7.5Mo \quad (2.1)$$

The microstructure of stainless steels can be predicted from the composition of strong ferrite and austenite promoters defined as the chromium(Cr_{eq}) and nickel (Ni_{eq}) equivalents by the empirical formulae from original plot of Schäffler diagram in Eq. 2.2 and 2.3 (Suutala*et al*., 1980):

$$Cr_{eq} = wiNi + 30wiC + 0.5wiMn \quad (2.2)$$

$$Ni_{eq} = wiCr + wiMo + 1.5wiSi + 0.5wiMn \quad (2.3)$$

Schäffler diagram has been modified several times since 1952 and combined work by Schäffler, Delong, Epsy, Hull, Hammar and Stevenson along with WRC-1992 and Chayes has been summarized in Bystram diagram (Suutala *et al*., 1979 and 1980 and Stoenescu *et al*., 2007). The formulae used to create Brystan's diagram are summarized in Table 2.2 (Lippold and Kotecki, 2005; Blondeau, 2008 and Bermejo, 2012). For proper use, the equivalency formulae must be chosen with respect to composition of the

selected steel, particularly in microstructure prediction for welding (Suutala *et al*., 1980 and Elmer, 1989).

Table 2.2 Summary of Modified Cr and Ni Equivalencies

Author	**Year**	**Cr_{eq} (wt%)**	**Ni_{eq} (wt%)**
Schäffler	1949	Cr +Mo +1.5 Si+0.5Nb	Ni+0.5Mn+30C+0.6Cu
De Long *et al.*	1956	Cr +Mo+1.5Si+0.5Nb	Ni+0.5Mn+30(C+N)
Epsy	1970	Cr+Mo+1.5Si+0.5Nb +5V+3Al	Ni+30C+x(N-0.045) +0.87+0.33Cu x = 30, if N = 0/0.20 x = 22, if N = 0.21/0.25 x = 20, if N = 0.26/0.35
Hull	1973	Cr+1.21Mo+0.48Si+0.14Nb +2.27V+0.72W+2.20Ti +0.21Ta+2.48Al	Ni+(0.11Mn-0.0086Mn^2) +24.5C+14.2N+0.41Co +0.44Cu
Hammar and Svennson	1979	Cr+1.37Mo+1.5Si+2Nb+3Ti	Ni+0.31Mn+22C +14.2N+Cu
WRC-1992/ Siewert*et al.*	1992	Cr+Mo+0.7Nb	Ni+35C+20N+0.2Cu

Figure 2.2 shows the Bystram diagram, including reference to the most recently developed stainless steels (Blondeu, 2008). Four possible major risk zones, notetably hot cracking, sigma phase formation, cold cracking and grain growth, have been notified, all play significant roles in the welding of stainless steels applications (Leber *et al*., 2007).

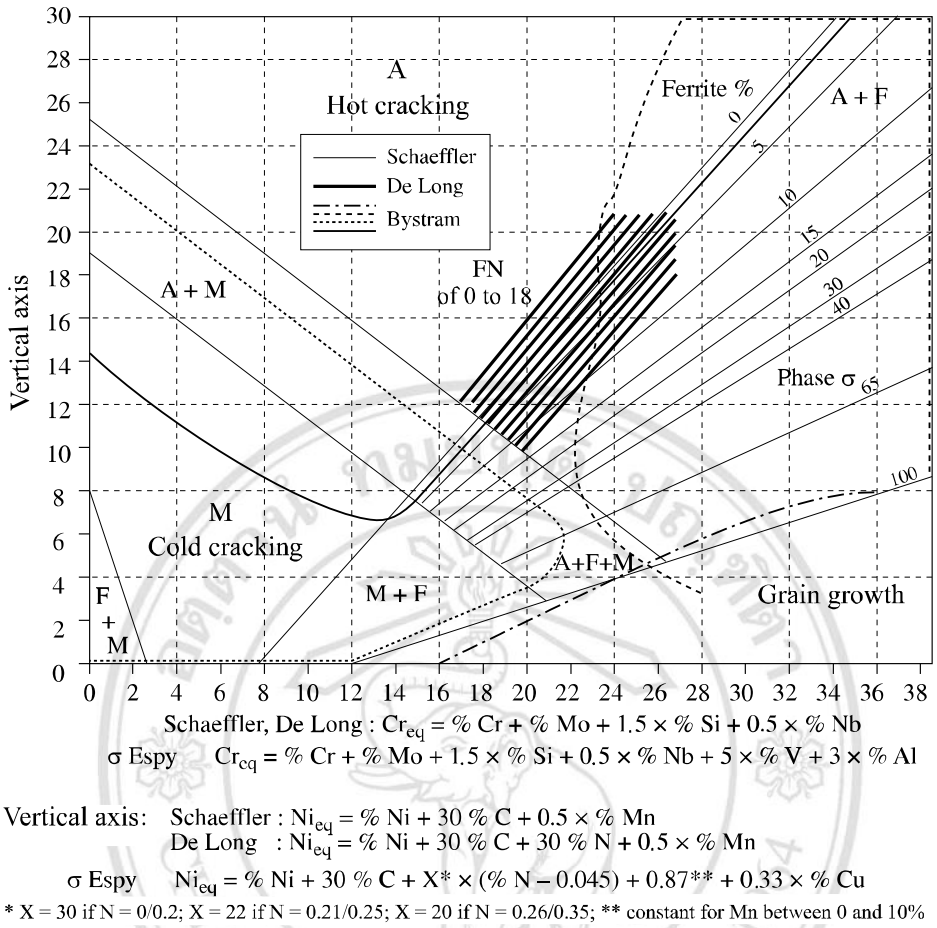

Figure 2.2 Fe-Cr Phase diagram from Brystan's work

A: austenite, M: martensite, F: ferrite, FN: ferrite number

(after Blondeu (2008)

For austenitic stainless steels, stacking fault energy can be estimated as summarized in Table 2.3.

Table 2.3 Stacking Fault Energy Estimation for Austenitic Stainless Steels

Author	Year	Stacking Fault Energy (mJ/m^2)
Leber*et al*.	2007	$25.7 + 2(\%Ni) + 410(\%C) - 0.9(\%Cr) - 77(\%N) - 13(\%Si) - 1{,}2(\%Mn)$
Poulon-Quin*et al*.	2009	$-53 + 6.2(\%Ni) + 10(\%C) - 0.7(\%Cr) + 3.2(\%Mn)$
Suzuki *et al*.	2009	$2.2(\%Ni) + 6(\%Cu) - 1.1(\%Cr) - 1.2(\%Mn) + 32$ when $(0.15 \leq C + N \leq 0.3)$
Tavares *et al*.	2009	$-53 + 6.2(\%Ni) + 10(\%C) - 0.7(\%Cr) + 3.2(\%Mn) + 9.3(\%Mo)$
Hamada *et al*.	2013	$16.7 + 2.1(\%Ni) + 26(\%Cu) - 0.9(\%Cr)$

2.2 The Mn-substituted Austenitic Stainless Steels

Austenitic stainless steels (ASSs) are the largest group and have been widely employed in many applications, including welding fabrications (Prasad *et al*., 2012). ASSs are characterized by FCC solid-solution austenite (Messler, 1999). Chromium content should be more than 15 wt% to preserve passive oxide protective film and nickel content should be 6-22 wt% to stabilize the austenite phase. The ratio of Fe to (Ni+Cr) is maintained at 70:30 to inhibit martensititic transformation (M_s) (de Dafé *et al*, 2003 and de Abreu *et al*., 2007).

Generally, nickel content in ASSs can be substituted by manganese in a proportion ratio of 1wt% Ni per 2 wt% Mn, while austenite is still retained as

predominant phase (Tavares *et al*., 2009). This Mn substituted group is called the 200 series ASSs (du Toit et al., 2012). The work-hardening and strength of the 200 series were reported to be higher than those of the 300 series. duToit*et al*. (2012) compared the AISI 202 and AISI 304 ASSs in terms of formability by Erichsen cupping test and uniaxial tensile tests at various angles to the rolling direction. Higher rate of work-hardening was found in AISI 202 ASSs indicating that more deformation-induced α′ martensite formation occurred than in AISI 304 ASSs and tensile properties were similar. Hence, it was considered to be possible to make use of AISI 202 as an alternative to AISI 304 ASSs.

Utilization of lower Ni-content ASSs in many applications became more widespread in Asian countries, especially in China and India (Charles, 2007). The combination of manganese with other alloying elements such as nitrogen and copper made the possibility in the reduction of nickel content with comparable properties in selected grades of the 200 series and with a lower price than the traditional 300 series, such that the 200 series could be used to produce welded tubes (Gavriljuk*et al*., 2000 and Razaee*et al*., 2011)

2.3 Welding Process for Thin Plate Austenitic Stainless Steels

A definition of welding by the American welding society is quoted as "The capacity of a material to be welded under fabrication conditions imposed into a specific, suitably designed structure and to perform satisfactorily in the intended service" (Lippold, 2015). Requirement of steel composition for pipeline welding to be used in seawater should acquire at least good resistance to general corrosion such as pitting and stress corrosion cracking (Alyousif and Nishimura, 2007). In terms of mechanical properties, the steel must withstand mechanical damage and have a practical durability in lifetime span service with practical cost in terms of pipe materials and fabrication process (Stephenson, 1987 and Baek *et al*., 2002).

The most applicable welding process to be used in pipeline applications is arc welding such as tungsten inert gas arc welding (TIGW) or gas tungsten arc welding (GTAW) process (Stephenson, 1987). Arc in the welding process is created from the applied electric current between two electrodes over ionized column of shielding gas,

preferably an inert one (Modenesi *et al*., 2000). Either helium or argon is normally used as the shielding/ protective gas at the electrode (Tridia *et al*., 2010). Shielding gas can be selected from Ar, Ar/He, Ar/N_2 or Ar/H_2, dependent on the expectation of best penetration according to parent metal, sheet thickness and weld seem geometry (Stephenson, 1987).

In tungsten arc welding, non-consummable tungsten-throriate (W-Th) has been permanently used as an electrode (Messler, 1999). There is no molten droplet pass through the tip and spill onto work surface. Therefore, it can be classified as clean process without any filler material requirement for thin sheet fabrication. Direct current (DC) or alternating current (AC) can be applied in this process with or without filler material (Davis, 1994). The choice of current and polarity depends on the process, the type of electrode, the arc atmosphere, and the metal being welded. A typical TIGW/GTAW process is illustrated in Figure 2.3.

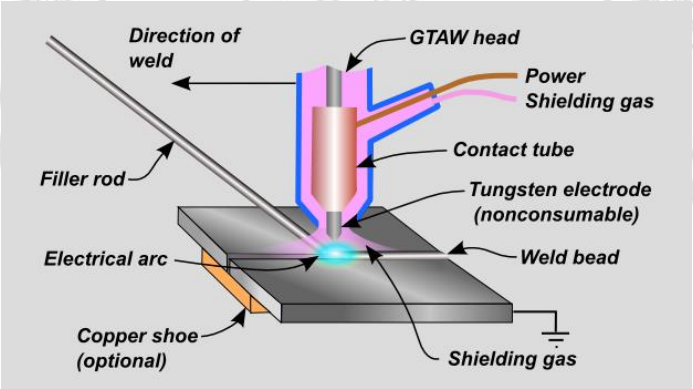

Figure 2.3 Schematic illustration of typical TIGW/GTAW process (after http://www.burnsstainless.com/Newsletters/Articles/Welding/GTAW_Figure_2.PNG)

To fabricate good quality and serviceable joints, there are two main processes to consider i.e. melting and solidification (Lippold, 2015). Both processes are affected by many parameters e.g. weld pool geometry, arc gap, flow rate, welding current, weld thermal cycles, welding speed, shielding gas, and cooling rate (Juang and Tarng, 2002; Tušek and Suban, 2000 and JamshidiAva *et al*., 2009).

The microstructure of weldment can be divided into three regions/zones including heat-affected zone (HAZ), fusion zone (FZ) and base metal zone (Stephenson, 1987).

Metallurgical phenomena occurring during weld solidification and cooling that affected microstructure and property of weldment are phase transformation, precipitation reactions, recrystallization and grain growth. These can occur in the three zones and the inter-boundaries between connected zones as shown in Figure 2.4 (Lippold, 2015).

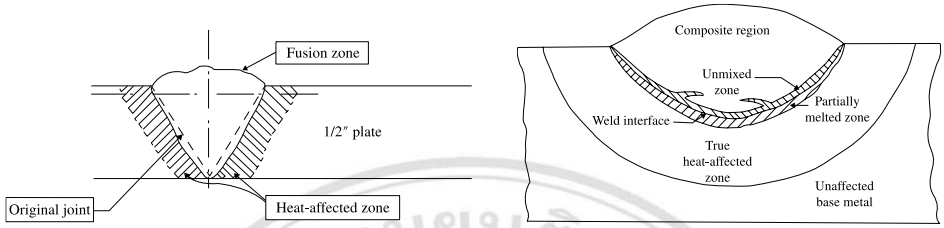

Figure 2.4 Regions of a fusion weld

(after Lippold (2015)

In general, the shape of weld beads, the weld pool shape and penetration are controlled by the Marangoni effect which results from (i) interaction of combined surface tension at the free surface of weld pool, (ii) applied welding current, (iii) buoyancy from aerodynamic drag force generated from shielding gas, and (iv) electromagnetic force generated from applied heat and fluid flow of weld surface, as illustrated in Figure 2.5 (Debroy and David, 1995;Modenesi *et al*., 2000 and Traidia *et al*., 2010). The penetration depth of a weld was also said to be sensitive to the change between compositions of weld parent (Debroy and David, 1995). The example of this was found in the case of 50% reduction in weld penetration when the sulfur composition in stainless steels was reduced from 0.010 to 0.003 wt% (Lippold, 2015)

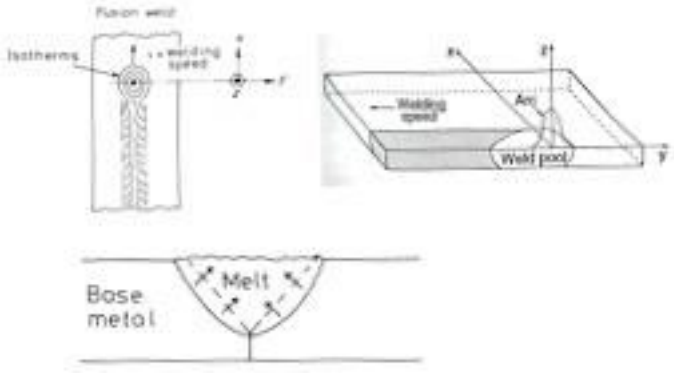

Figure 2.5 Illustrations of isotherms about the heat sources in fusion welding, the shape of weld beads, the weld pool shape and penetration

(after Clarke *et al*. (1999) and Porter and Easterling (2004)).

Bead contour and adequate penetration depth can be controlled by applying a high level of peak current. Weld arc stability can be sufficiently maintained by low level background current and reduced plate distortion (Park *et al*., 2009 and Pal and Pal, 2011). Higher welding speed will create tear drop shape at the bead front, while lower speed results in elliptical shape, as illustrated in Figure 2.6 (Lippold, 2015).

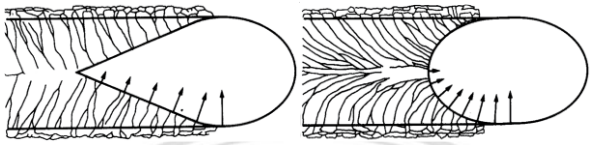

Tear drop Elliptical

Figure 2.6 Illustration of tear drop and elliptical bead front

(after Lippold, 2015)

2.3.1 Pulsed Current TIG Arc Welding or Gas Tungsten Arc Welding for Thin Plate Welding without Filler

During conventional arc welding, it is generally to control weld solidification in fusion zones, especially to prevent coarse columnar grains which increase hot cracking susceptibility (Karunakaran and Balasubramanian, 2011). To refine the fusion zone, pulsed current TIG arc welding or gas tungsten arc welding (PCTIGW/PCGTAW) is preferred with only minor modification of the conventional equipment (Senthil Kumar *et al*., 2007).

Grain size refinement in FZ, HAZ width reduction, segregation control, and better heat input control had been accomplished by means of optimized PCGTAW process parameters including pulsed current, background current, percentage on time and pulse frequency, which can narrow down HAZ width providing the highest pitting corrosion resistance (Lothongkum *et al*., 2001;Yousefieh*et al*., 2011 and Pal and Pal, 2011).

2.3.2 Pulsed Current TIG Arc Welding or Gas Tungsten Arc Welding for Thin Plate Welding without Filler

Two main parameters to be reviewed here are (i) cooling rate during solidification and (ii) shielding gas in the TIGW/GTAW process, since they have significant effects on microstructure in heterogeneous zones of welded ASSs and hence on properties of welded joints.

- **Cooling Rate**

Thermal contraction through weld solidification can be controlled by producing a dual structure called duplex matrix i.e. δ-ferrite retained within austenite (γ) (Vitek *et al*., 1995 and Lin and Chen, 2001). Lothongkum *et al*. (1999 and 2001) showed that the control of weld metal ferrite content in order to maintain resistance to weld solidification cracking could be monitored by ferrite number (FN), such that when FN is higher than 3 then cracking can be prevented. The level of residual ferrite in ASS weld zones depends on the applied cooling rate. Effects of cooling rates found in the fusion zone of Fe-Cr-Ni stainless steel by Elmer *et al*. (1990) were in agreement to those in AISI 304 and 316L found by Rodrigues and Loureiro (2004). Apart from ferrite content, high heat input current tends to reduce the cooling rate, thus promotes coarsening of δ-ferrite dendrites and results in a decrease of weld hardness. Therefore, the δ-ferrite content and morphology must be closely monitored and controlled in order to maintain weld ductility, toughness, corrosion resistance and hot cracking resistance (Pujar, *et al*., 1999, Lin and Chen, 2001)

- **Shielding Gas**

Shielding gas plays an important role in arc welding of highly alloyed materials, such as austenitic, ferritic, martensitic, duplex and superduplex stainless steels (Tušek and Suban, 2000). It affects arc shape, materials transfer, melting rate and energy distribution in the arc (Suban and Tušek, 2001). Normally, the TIGW/GTAW employs pure argon as a

shielding gas to sustain arc stability and to acquire fairly low spatter (Deepashri *et al*., 2006 and Huang, 2009). Partially-mixed hydrogen-argon gases were introduced in arc welding with hydrogen content around 0.5 to 5 Vol. % (v. d. Mee *et al*., 1999). Tušek and Suban (2001) found that a small amount of hydrogen maintained arc power due to high thermal conductivity, narrowed the arc gap, and increased the energy concentration, thus gave deeper weld penetration (Durgutlu, 2004). However, the increase in hydrogen content can cause detrimental effects to mechanical properties from e.g. gas bubbles, and can generate cracking in the welding process (Tušek and Suban, 2000 and Durgutlu, 2004). As nitrogen can act as a strong austenite promoter being around 20-30 times more effective than nickel (Tseng and Chou, 2003), therefore, mixed nitrogen-argon gases were also utilized as a shielding gas for arc welding of ASSs (Huang, 2009). The beneficial effects of nitrogen addition in shielding gas are to increase nitrogen content in ASS weldment and to decrease the retained ferrite level, which tends to cause welding distortion (Tseng and Chou, 2003).

2.4 Solidification of Weld Fusion Zones in Austenitic Stainless Steels

2.4.1 Pulsed Current TIG Arc Welding or Gas Tungsten Arc Welding for Thin Plate Welding without Filler

In weld deposits of ASSs, solidification can proceed with a cellular front, subsequently resulting in columnar–grain shape (Bhadeshia, 2001). The majority of the growth direction of austenite grains is influenced by the orientation of the δ-grains, which solidify as primary δ-ferrite in chromium-rich stainless steel (Koseki *et al*., 1995). Upon cooling, the outer portion of dendrites having lower chromium content transformed into γ-austenite, while dendritic core appeared as vermicular or skeleton form, or even as dual morphology (Kokawa *et al*., 1989). The primary phase in the alloys can be predicted from Cr and Ni equivalencies summarized in Table 2.2 and Schäffler/Bystram diagram in Figure 2.2.

The maximum volume percentage of δ-ferrite at ambient temperature as determined from weld microstructure must fall within range of 6-8 vol%. If ferritscope is employed, the ferrite content can be presented as ferrite number (FN) and should fall within a range of 3 to 12 (Lothongkum *et al*., 2001) or around 3 to 4 (Bermejo, 2012).

2.4.2 Pulsed Current TIG Arc Welding or Gas Tungsten Arc Welding for Thin Plate Welding without Filler

2.4.2.1 Microstructure Classification by Cr- and Ni-equivalency Ratio

Takalo *et al*. (1979) and Suutala *et al*. (1979 and 1980) had classified morphology expected to appear in welded ASSs based onCr_{eq}/Ni_{eq}ratio as follows:

Type A: Cr_{eq}/Ni_{eq} ratio ≤ 1.48

The leading phase is austenite due to the relatively high nickel content. δ-ferrite solidified in the rest of melt in cellular form, running from bottom of weld to the surface with the growth direction of [100]ferrite. The final microstructure may contain roundish vermicular ferrite in regard to its formation mechanism from eutectic transformation.

Type B: Cr_{eq}/Ni_{eq} ratio ≤ 1.95

The majority of structure consists of irregular morph due to the lack of self-evident growth units. Fine structure of dispersed ferritic-austenitic or duplex structure may be observed. δ-ferrite is situated mainly at the axes of the cells or dendrites, so the final microstructure exists in either vermicular or lacy (or lathy) form as shown Figure 2.7.

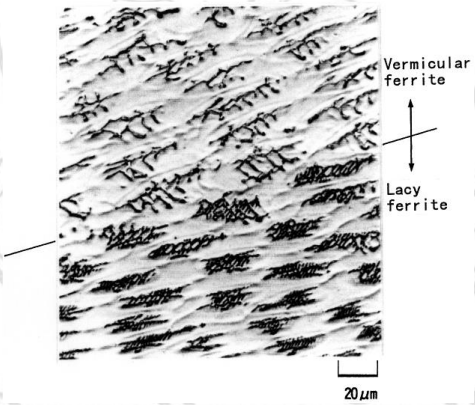

Figure 2.7 Morphology of vermicular and lacy (lathy) ferrite in weld microstructure of austenitic stainless steels (after Inoue and Koseki, 2007)

Type C: Cr_{eq}/Ni_{eq} ratio ≥ 1.95

Generally, this structure can be distinguished by the large growth units or austenite blocks containing lathy ferrite morphology. Dominant growth mechanism is cellular or cellular-dendritic substructure. Orientation relation between austenite and lathy ferrite is either Kurdjumov-Sachs (K-S) or Nishiyama-Wasserman (N-W) or even lies in between both.

Microstructure types and the amount of δ-ferrite in structure of welded ASSs as predicted by the Schäffler diagram are indicated in Figure 2.8.

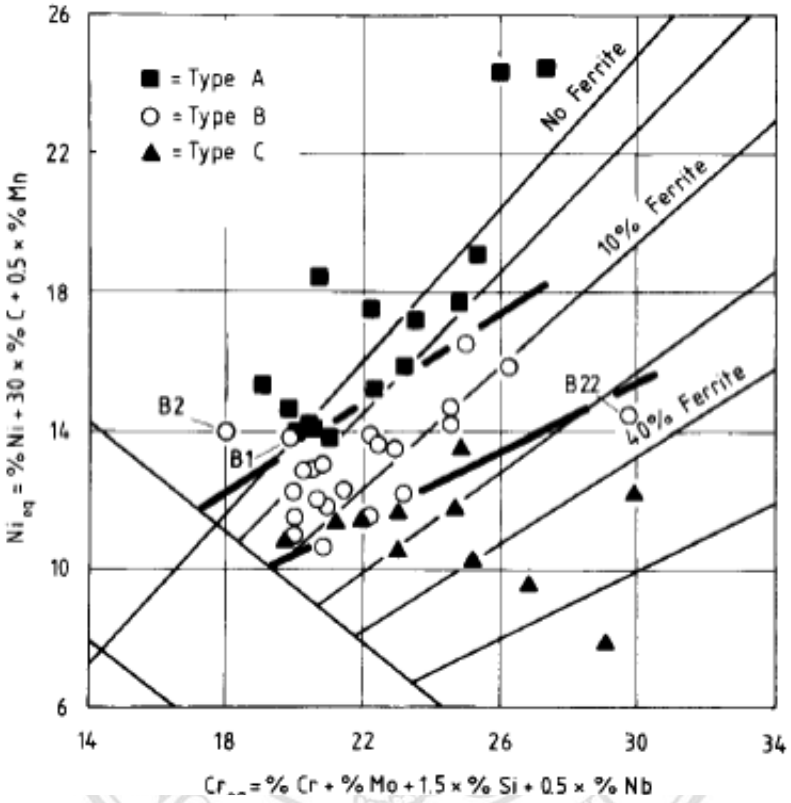

Figure 2.8 Microstructure types and the amount of δ-ferrite in structure of welded austenitic stainless steels as predicted by the Schäffler diagram

(after Suutala *et al*., 1980)

2.4.2.2 Primary Solidification Modes in Welded Austenitic Stainless Steels

Solidification mechanism in the welding process of ASSs can also be classified by solidification behavior in the fusion zone (Arata *et al*., 1976 and 1977; Vitek *et al*., 1995; Elmer, 1989; Inoue and Koseki, 2007) and summarized in Table 2.4, Table 2.5 and Figure 2.9.

Table 2.4 Notation

Symbol	Description
A_P	Primary austenite which solidifies from the A or AF mode
A_E	Second-phase (eutectic) austenite which solidifies from FA mode
A_T	Austenite which forms during the solid-state transformation of ferrite by diffusion-controlled growth of austenite from ferrite/austenite boundaries
A_M	Austenite which forms during the solid-state transformation of ferrite by a massive phase transformation within ferrite matrix
F_P	Primary ferrite which solidifies from the F or FA mode
F_E	Second-phase (eutectic) ferrite which solidifies from FA mode

Table 2.5 Solidification Mode, Solidification Sequence, and Solid-State Transformation Responsible for Variation in Morphology in Fusion Zone of Welds Austenitic Stainless Steels

Solidification mode	**Solidification sequence**	**Solid-State Transformation**	**Morphology**
A	$L \rightarrow (L + A_P) \rightarrow A$ Arata*et al.*(1976), Elmer (1989) and Lippold and Kotecki (2005)	none	cellular-dendritic A cellular A
AF	$L \rightarrow (L+ A_P) \rightarrow (L+ A_P+ F_E) \rightarrow (A_P+ F_E)$ Elmer (1989) and Lippold and Kotecki (2005)	$F_E \rightarrow A_T$	interdendritic F intercellular F
E	$L \rightarrow (L+ F_E+ A_E) \rightarrow (F_E+ A_E)$ Elmer (1989)	$F_E \rightarrow A_T$	eutectic
FA	$L \rightarrow (L+ F_P) \rightarrow (L+ F_P + A_E) \rightarrow (F_P+ A_E)$ Elmer (1989), Lippold and Kotecki (2005), Kosek*i et al*. (1999), Shangar *et al*. (2003) and Inoue *et al*. (2007)	$F_P \rightarrow A_T$	intercellular A vermicular F lacy F blocky A
F	$L \rightarrow (L+ F_P) \rightarrow F_P$ Elmer (1989) and Lippold and Kotecki (2005)	$F_P \rightarrow A_W$ $F_P \rightarrow A_M$ None	Widmanstätten A massive A cellular F

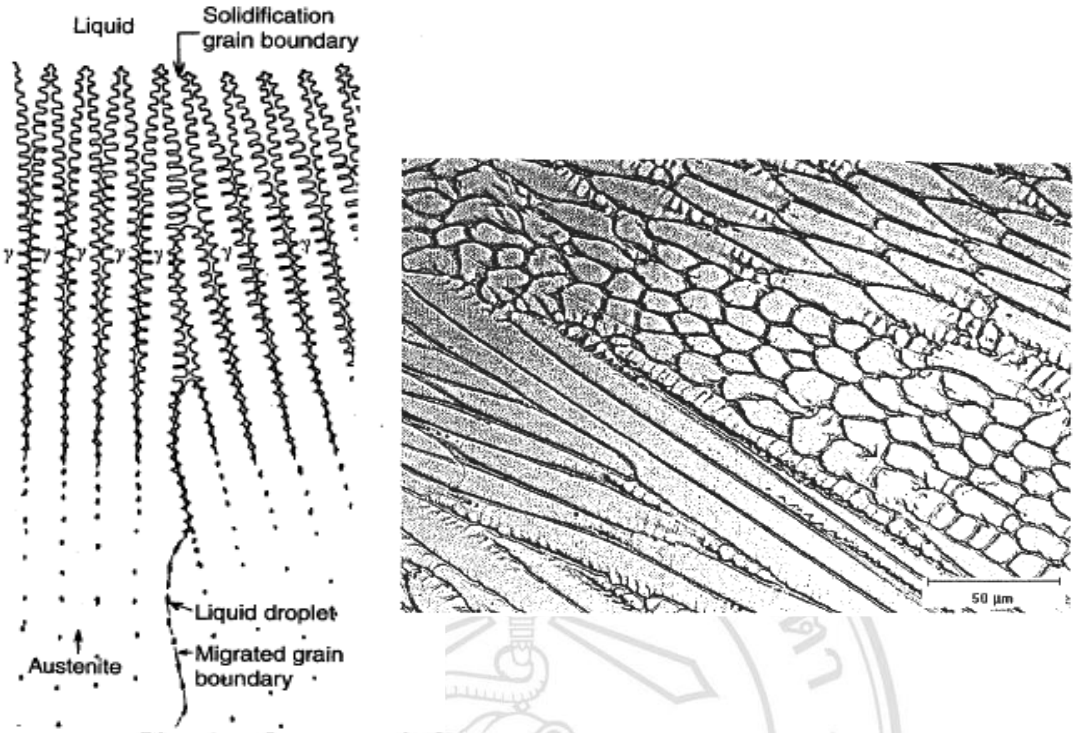

(a) Type A, fully austenite (after Lippold and Kotecki, 2005)

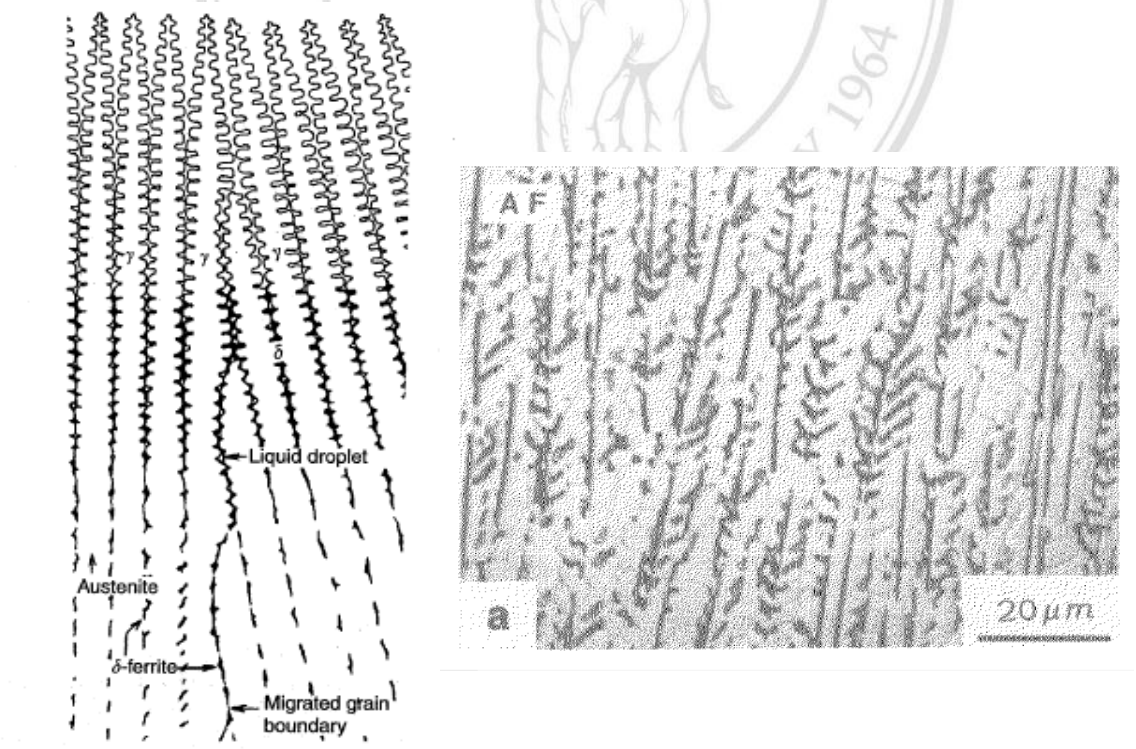

(b) Type AF (after Lippold and Kotecki (2005))

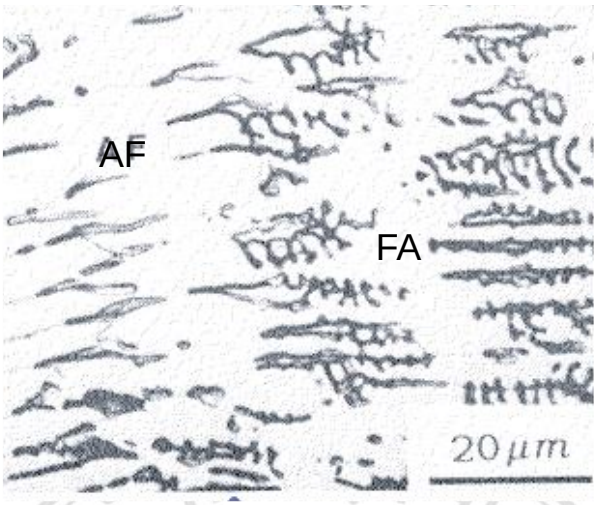

(c) Type E (after Elmer *et al*., 1990-a)

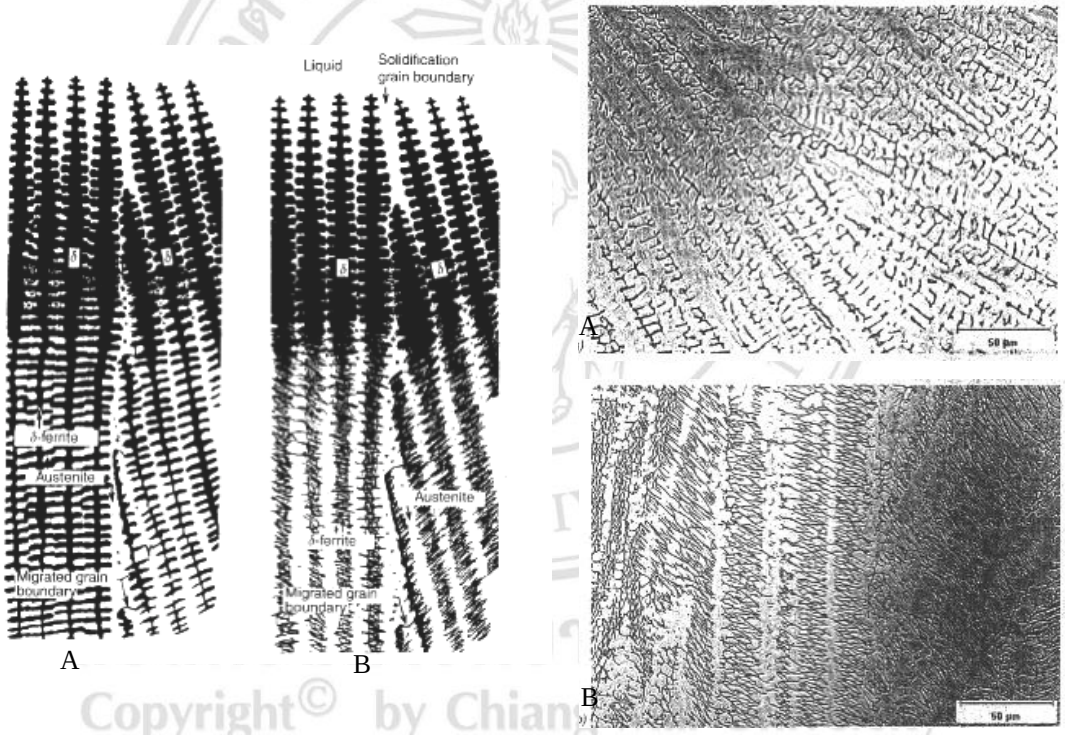

(d) Type FA: (A) skeletal ferrite and (B) lathy ferrite

(after Lippold and Kotecki (2005))

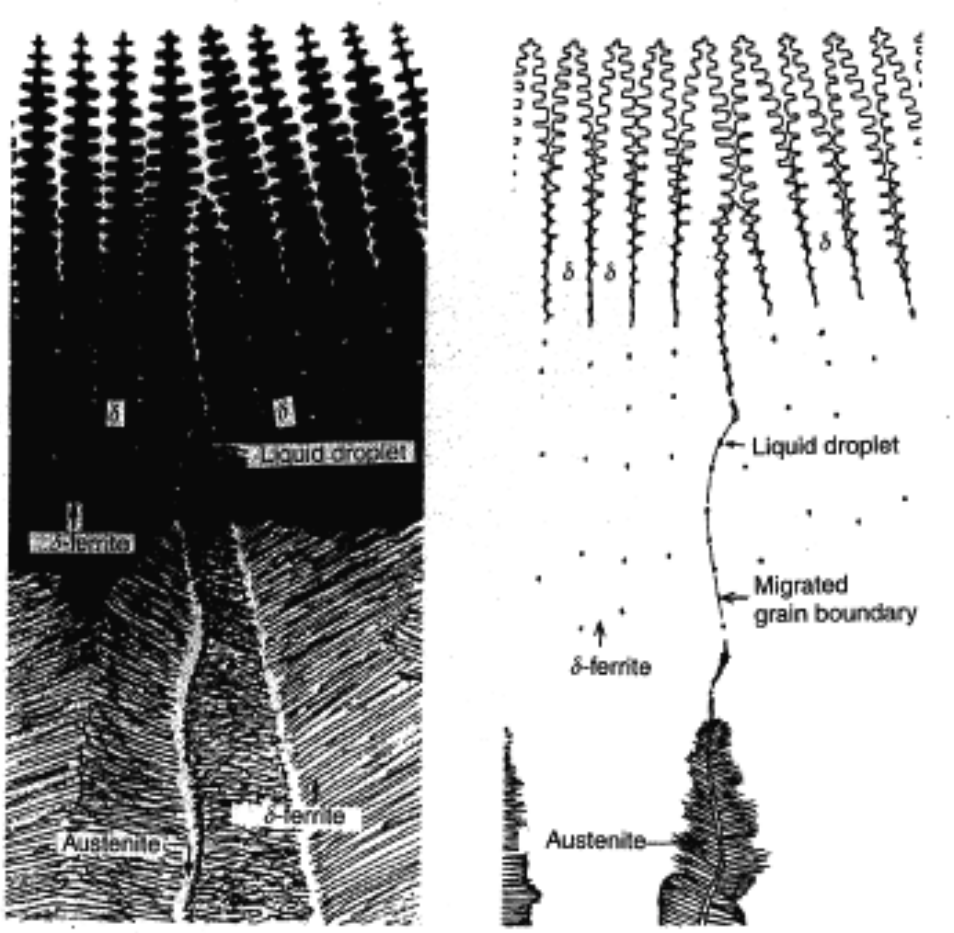

(e) Type F (after Lippold and Kotecki (2005))

Figure 2.9 Solidification mode in fusion zone of welds austenitic stainless steels

2.5 Corrosion of Stainless Steels and Weldment

Stainless steels have chromium oxide protective film, but they still have susceptibility to corrosion from film break down. When surface of steels exposes to elevate temperature or severe acidic environment, localized corrosion attack can be found at the grain boundary from depletion in chromium adjacent to chromium-rich carbides or nitride. In cold-roll steel sheet, it is known that prior cold-working can the initiate IGC susceptibility and pitting corrosion (Peguet *et al*., 2007).

The relationship between potential and current during corrosion process of stainless steels can be divided into three main stages i.e. active stage, passivation stage and transpassivation stage, as shown in Figure 2.10. Reactions of Cr_2O_3 film formation, passive film dissolution as positive chromium ions and transpassive film dissolution as negative chromium ions can be written (Sato, 2011) as shown in Eq. 2.4 to 2.6, respectively:

$$2Cr^{3+} + 3H_2O \longrightarrow Cr_2O_3 + 6H^+_{aq} + 6e^-_M \quad \text{passive film formation} \quad (2.4)$$

$$Cr_2O_3 + 6H^+ \longrightarrow 2Cr^{3+} + 3H_2O \quad \text{passive film dissolution} \quad (2.5)$$

$$Cr_2O_3 + 5H_2O + 6e^-_M \longrightarrow 2CrO^{2-}_{4,aq} + 10H^+_{aq} \quad \text{transpassive film dissolution} \quad (2.6)$$

Corrosion potential (E_{corr}) and corrosion current density (i_{corr}) can be determined from intercept between anodic and cathodic Tafel slopes (Ha *et al*., 2009). Generally, electrode potential of metal anode in passivation stage is stable within range before film break down, it is called passive potential, as shown in Figure 2.10. When potential reaches transpassivation stage, potential at this point is called transpassivation potential or pitting potential or breakdown potential (E_t or E_p or E_b).

Pitting will start to occur above this potential level. Passivity break down in stainless steel and pit initiation usually occur at the nonmetallic MnS inclusion sites. The reverse scan will give repassivation potential (E_{pr} or E_{rp}), below which repassivation occurs. Resistance of passive film may be defined also by the area of the hysteresis loop (red elliptical mark) i.e. the difference between the breakdown potential and the repassivation potential ($E_b - E_{rp}$).

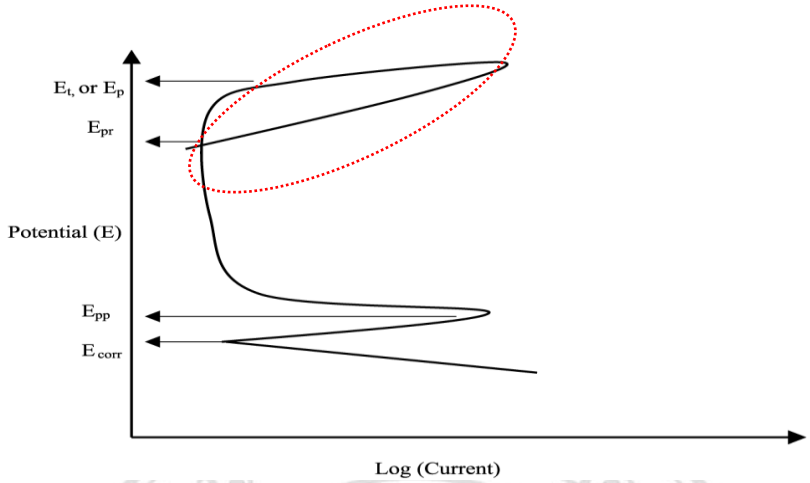

Figure 2.10

Potential stages during passive film break down and pitting isoccurred.

E_{corr} = corrosion potential,

E_{pp} = primary passivation potential,

E_t or Ep or Eb = transpassivation potential or pitting potential or breakdown potential, E_{pr} or E_{rp} = repassivation potential

(after Sato (2011) and http://origin-ars.els-cdn.com/content/image/1-s2.0-S0925838804005006-gr13.gif)

In aggressive chloride containing environment, the passive film can be broken from dissolution at local sites, pits are created and corrosion products are released (Sourisseu *et al.*, 2005), as illustrated in Figure 2.11.

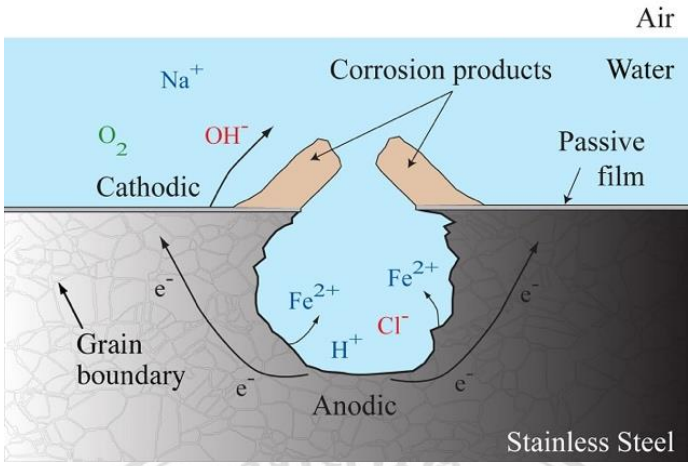

Figure 2.11 Illustration of pitting corrosion forming at deteriorated sites in protective film of stainless steels

(after https://cdn.comsol.com/wordpress/2014/09/corrosion-diagram.jpg)

To include the effect of Mn to pitting corrosion resistance (PCR), Rondelli *et al*., 1995 had proposed equation (2.7) for pitting resistance prediction as the pitting equivalent number ($PREN_{Mn}$) as follows:

$$PREN_{Mn} = Cr + 3.3Mo + 30N - Mn \quad (2.7)$$

The prediction from this equation can be used to compare with actual PCR derived from the Tafel plot in cyclic potentiodynamic polarization curves.

For intergranular corrosion (IGC) resistance in stainless steels, electrochemical potentiokinetic reactivation (EPR) test is the means to find degree of sensitization (DOS) from the polarization of cyclic voltammograms. This test focuses on the cause of intergranular corrosion in stainless steels from chromium depletion with regards to precipitation of complex chromium carbide. The test assumption is based on that sensitization occurs at the grain boundaries due to chromium depletion, while grain bodies remain unsensitized.

The amount of reactivation is mainly depending on chromium content in the solid solution as suggested by Aydoğdu and Aydinol (2006). Methodology of double loop electrochemical potentiokinetic reactivation (DL-EPR) has been developed in order to

quantify the better results of non-destructive sensitization test in stainless steels (Kain*et al*. (2005); Aydoğdu and Aydinol (2006) and Pardo *et al*. (2007)). The nose of peak current on the anodic scan in Figure 2.12 is assumed as the activation peak current (I_a), while the nose on the reverse scan is the re-activation current (I_r) is related to preferential break down of the passive film covering the chromium-depleted grain boundary zones of the stainless steels. All quoted potentials are referred to the SCE scale as stated by de Lima-Neto *et al*. (2008) and Friere *et al*. (2008). DOS can be calculated from the ratio of I_r/I_a in Eq. 2.8 after Rahimi*et al*. (2011):

$$DOS = I_r / I_a \qquad (2.8)$$

where I_r= maximum current density of the re-activation curve (μA.cm^{-2}) and I_a is maximum current density of the anodic polarization curve (μA.cm^{-2}). Generally, two DL-EPR loop shapes can be classified as nonsensitized and sensitized in Figure 2.13.

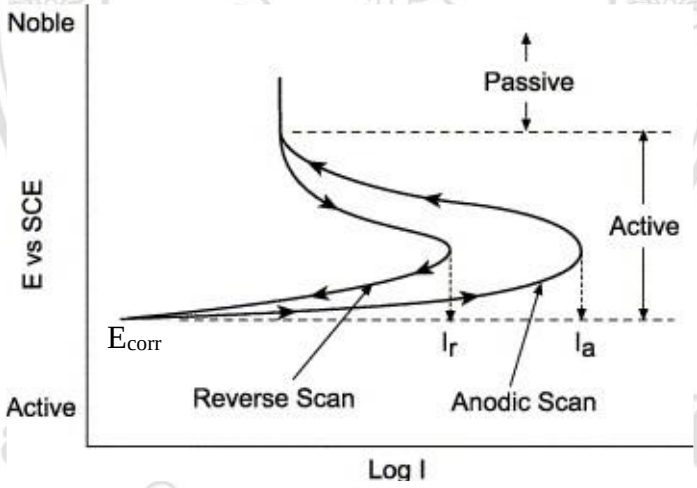

Figure 2.12 Double loop electrochemical potentiodynamic reactivation (DL-EPR) methodology according to ASTM G108 for determining degree of sensitization (DOS) in ASSs

(after Aydoğdu and Aydinol (2006)).

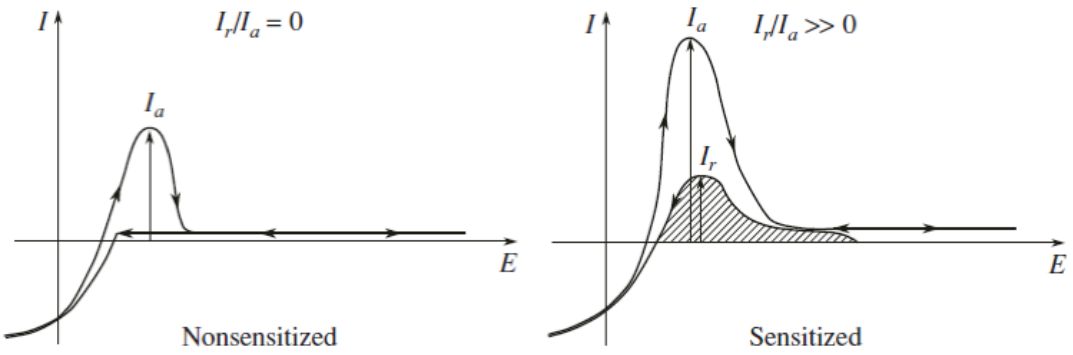

Figure 2.13 DL-EPR loop shapes (after Kiraa*et al*. (2007))

Degree of sensitization (DOS) or susceptibility to intergranular corrosion in austenitic stainless steels can also be determined from micrographs. The observation at grain boundaries after performing cyclic potentiodynamic polarization test is described in several ASTM standard practices. Sensitization at grain boundaries can be observed from an appearance of etches at grain boundaries or at ferritic dendrites. To categorize the type and severity of sensitization, sensitized microstructure can be compared with a reference structure. Microstructure after perform cyclic polarization tests from guidance of ASTM A262-2008 was shown in Figure 2.14.

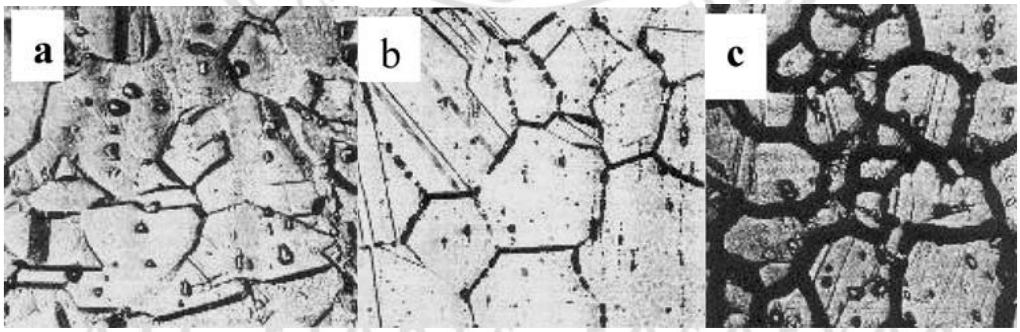

(a) step (b) dual (c) ditch

Figure 2.14 Classification of sensitized microstructure according to ASTM A262-2008. Only step, dual or mixed step and dual types are acceptable.

(after Lima *et al*. (2005))

Calculation of normalized charge (P_a) is another method to indicate resistance to intergranular corrosion. Normalization charge (P_a) can be obtained from Eq. 2.9 after Záhumenský *et al*. (1999):

$$P_a = (Q/X) \tag{2.9}$$

where P_a= normalized charge, Q = measured charge from current integration, X = ASTM E112 grain size number (G) i.e. $X = A_s[5.1 \times 10^{-3} e^{-0.35}]$ and A_s= exposing area to the electrolyte (cm2) of tested specimens.

In general, corrosion behavior of stainless steel weldments, such as interdendritic pitting and intergranular corrosion cracking (IGC), can be evaluated also by standard practices e.g. in ASTM A262, G48, G5 and G108 (Garcia *et al*., 2008-a). Microstructural observation after local electrochemical impedance spectroscopy (LEIS) from the weld string to HAZ in TIG welded AISI 304 stainless steel by de Lima-Neto *et al*. (2008) revealed ditches at grain boundaries in HAZ and cyclic potentiodynamic tests showed the remarkably worse pitting corrosion resistance in the HAZ than in the base metal. Lo *et al*. (2009), Padhy *et al*. (2010) and Metikoš-Huković *et al*. (2011) proposed a possible way to improve pitting corrosion resistance via addition of alloying elements i.e. copper together with nitrogen and molybdenum. Gooch (1996) and Jagerlius-Pettersson (1999) had earlier suggested that nitrogen and molybdenum might not have a strong influence on inhibition of pit initiation, but could instead slow the anodic dissolution rate and improve repassivation kinetics.

2.6 Micro-Vickers Hardness (MVH) of Weldment

Hardness of welded specimen is affected by several factors e.g. the composition of the base metal and the weld metal, the metallurgical effects of the welding process and cooling rate, cold working of the metal, heat treatment (Lippold and Kotecki, 2005). Micro-Vickers Hardness (MVH) can be determined by forcing a square-based pyramid, diamond indenter into a flat surface of welded specimens. Predetermined load to be used in hardness testing must be calibrated prior to perform the indentation. Indenter layout and mean diagonal measurement are illustrated in Figure 2.15.

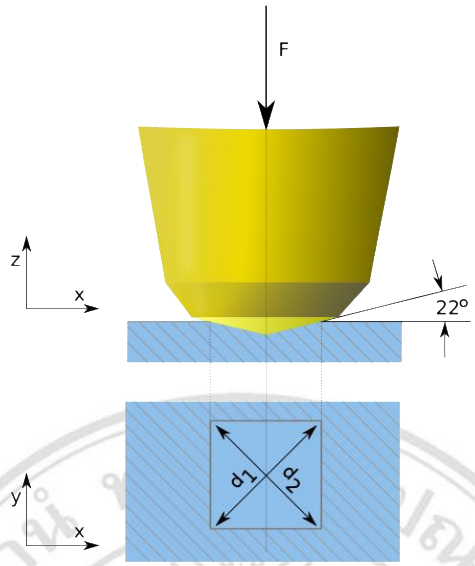

Figure 2.15 Illustration of micro-Vickers indenter layout and mean diagonal measurement following ASTM E384 standard practice.

2.7 Tensile Properties of Weldment

In weld fabrication process, tensile properties at base metal, weld metal and at the conformity of heat affected zone (HAZ) are very important and must put into consideration. Design of weld joint requires only minimum amount of weld metal as to conserve the ductility, which is important in the pipeline applications. Minimum distortion and lowest residual stress caused by weld metal shrinkage during solidification, thermal expansion and contraction under harsh temperature gradients, are required (Messler, 1999; Lippold and Kotecki, 2005 and Blondeau, 2008). Normally welded joint specimens are in rectangular shape. To determine tensile strength of welds, maximum load is divided by the cross-section area prior the deformation to be occurred and in unit of stress per cross-sectional area following the method by Grimm *et al*. (2000). A universal testing machine can be used to perform tensile test and tensile strength can be obtained from Eq. 2.10 as follows:

$$\text{Tensile strength} = F/(d \times W) \tag{2.10}$$

Where $F =$ maximum force (N), $d =$ gauge length (mm) and W = thickness (mm)

As previously mentioned, the presence of δ-ferrite has a crucial impact on mechanical properties (Lee *et al*., 2009-b). The Cr_{eq}/Ni_{eq}ratio can be employed to estimate the amount of δ-ferrite. Higher Cr_{eq}/Ni_{eq}ratio predicted an increase in the δ-ferrite content and hence an increase in strength. Kuo *et al*. (2007) had reported the contribution of supercooling effect in vibration welding that can block the growth of δ-ferrite, resulting in fine and short dendrite arm of δ-ferrite, reducing the residual stress at proper vibration time. Effect of heat input also contributed to tensile properties of welded AISI 304 (Kumar *et al*., 2011). Higher heat input enlarged the width of FZ and HAZ, and induced grain coarsening. Lower heat input produced fine dendrite structure and provided maximum tensile strength and ductility.